

Deep Learning-based Attenuation Correction Improves Diagnostic Accuracy of Cardiac SPECT

Running title: AI-based SPECT attenuation correction

Aakash D. Shanbhag MSc^{1*}, Robert J.H. Miller MD^{2*}, Konrad Pieszko MD, PhD³, Mark Lemley BS¹, Paul Kavanagh MSc¹, Attila Feher MD, PhD⁴, Edward J. Miller MD, PhD⁴, Albert J. Sinusas, MD⁴, Philipp A. Kaufmann, MD⁵, Donghee Han, MD¹, Cathleen Huang BA¹, Joanna X. Liang BA¹, Daniel S. Berman MD¹, Damini Dey PhD¹, Piotr J. Slomka PhD¹

1. Departments of Medicine (Division of Artificial Intelligence in Medicine), Imaging and Biomedical Sciences, Cedars-Sinai Medical Center, Los Angeles, CA, USA
2. Department of Cardiac Sciences, University of Calgary, Calgary AB, Canada
3. Department of Interventional Cardiology and Cardiac Surgery, University of Zielona Gora, Poland
4. Section of Cardiovascular Medicine, Department of Internal Medicine, Yale University School of Medicine, New Haven, CT, USA
5. Department of Nuclear Medicine, Cardiac Imaging, University Hospital Zurich, Zurich, Switzerland

*Authors contributed equally

Word count: 4975 (including all elements)

Corresponding Author:

Piotr J. Slomka, PhD
Cedars-Sinai Medical Center
8700 Beverly Blvd, Suite Metro 203
Los Angeles, CA 90048
Email: Piotr.Slomka@cshs.org

First Author:

Aakash D. Shanbhag, MSc
Cedars-Sinai Medical Center
8700 Beverly Blvd, Suite Metro 203
Los Angeles, CA 90048
Email: Aakash.Shanbhag@cshs.org

Funding: This research was supported in part by grants R01HL089765 and R35HL161195 from the National Heart, Lung, and Blood Institute/ National Institutes of Health (NHLBI/NIH) (PI: Piotr Slomka). The content is solely the responsibility of the authors and does not necessarily represent the official views of the National Institutes of Health.

ABSTRACT (330 words)

Introduction

To improve diagnostic accuracy, myocardial perfusion imaging (MPI) SPECT studies can use CT-based attenuation correction (AC) (CTAC). However, CTAC is not available for most SPECT systems in clinical use, increases radiation exposure, and is impacted by misregistration. We developed and externally validated a deep-learning model to generate simulated AC images directly from non-attenuation corrected (NC) SPECT, without the need for CT.

Methods

SPECT MPI was performed using Tc-99m sestamibi or Tc-99m tetrofosmin on contemporary scanners with solid-state detectors. We developed a conditional generative adversarial neural network that generates simulated AC SPECT images (DeepAC). The model was trained with short-axis NC and AC images performed in one site (n=4886) and was tested in patients from two separate external sites (n=604). We assessed diagnostic accuracy of stress total perfusion deficit (TPD) obtained from NC, AC, and DeepAC images for obstructive coronary artery disease (CAD) with area under the receiver operating characteristic curve (AUC). We also quantified direct count change between AC, NC, and DeepAC images on a per-voxel basis.

Results

DeepAC could be obtained in <1 second from NC images, AUC for obstructive CAD was higher for DeepAC TPD (0.79, 95% CI 0.72 – 0.85) compared to NC TPD (0.70, 95% Confidence Intervals (CI) 0.63 – 0.78, p<0.001), and similar to AC TPD (0.81, 95% CI 0.75 – 0.87, p=0.196). The normalcy rate in the LLK population was higher for DeepAC TPD (70.4%) and AC TPD (75.0%) compared to NC TPD (54.6%, p<0.001 for both). Positive count change (increase in

counts) was significantly higher for AC vs NC (median 9.4, Inter Quartile Range (IQR) 6.0 – 14.2, $p < 0.001$) than for AC vs DeepAC (median 2.4, interquartile range [IQR] 1.3 – 4.2).

Conclusion

In an independent external dataset, DeepAC provides improved diagnostic accuracy for obstructive CAD similar to actual AC, as compared to NC images. DeepAC simplifies the task of artifact identification for physicians, avoids misregistration artifacts, and can be performed rapidly without the need for CT hardware and additional acquisitions.

KEYWORDS:

Attenuation correction, SPECT, myocardial perfusion imaging, deep learning, artificial intelligence

INTRODUCTION

SPECT myocardial perfusion imaging (MPI) is frequently used to evaluate patients for the presence of obstructive coronary artery disease (CAD) (1). Abnormalities of regional perfusion are used to identify patients with a higher likelihood of having obstructive CAD (1,2). However, perfusion abnormalities can be similar in appearance to soft-tissue photon attenuation artifacts.

CT can be used to provide attenuation correction (AC) (CTAC) (3) and has been shown to improve the diagnostic accuracy of SPECT MPI and increase specificity from 81% to 88% (4). AC imaging has been proposed as an important method to significantly increase the proportion of patients who are candidates for rest scan cancellation (5). However, CTAC requires dedicated, expensive SPECT/CT scanners and is associated with additional radiation exposure. Importantly, misregistration of the separately acquired SPECT and CTAC maps is often a source of artifacts, which needs careful quality control and can potentially diminish the clinical value of AC images (6). For these reasons, despite its advantages, CTAC is currently performed in a minority of SPECT MPI scans. This is especially true for the latest generation of solid-state scanners where CTAC is performed in <5% of sites (personal communication) and is available only from one vendor.

To provide the benefits of AC without the above shortcomings, we developed and evaluated a deep learning model (DeepAC) which applies AC directly to non-corrected (NC) short-axis images, without the use of CT (or the need of re-reconstruction of the data), by generating simulated AC images. DeepAC is a conditional generative adversarial network (cGAN) which is comprised of two competing networks. A generator is tasked with creating DeepAC images while the discriminator differentiates the DeepAC images from actual AC images. The process is repeated until the discriminator network is no longer able to differentiate real AC images from

fake AC images. Importantly, by generating DeepAC SPECT images, physicians may be able to better evaluate images for potential artifacts and myocardial segmentation errors.

In this study, we compared image quantification using non-attenuation corrected (NC) images to CT-based AC and DeepAC images. In an independent external dataset, we compared the diagnostic accuracy of quantitative perfusion analysis for obstructive CAD, DeepAC, NC, and CT-based AC imaging. We also performed change analysis to better understand the potential improvement in DeepAC images compared to actual AC images.

MATERIALS AND METHODS

Patient Populations

We included two separate populations from separate centers. The model was trained with 4886 patients (45% female) from a single center (Yale University) who underwent SPECT MPI with CTAC (details in Supplemental Table 1). The model was then tested in an external population of 604 patients (48% male) from two different centers (University of Zurich and University of Calgary). All data and images were de-identified and transferred to Cedars-Sinai. The study protocol complied with the Declaration of Helsinki and was approved by the institutional review boards at each participating institution. The overall study was approved by the institutional review board at Cedars-Sinai Medical Center. Written informed consent or waiver of consent was obtained at each institution.

SPECT Image Acquisition

All scans were performed per SPECT/CT MPI guidelines (7), and only stress images were used in the present analysis. In the training population, patients underwent stress-rest/stress-only

(n=4112, 84%), rest-stress (n=684, 14%), or two-day (n=90, 2%) imaging using ^{99m}Tc -tetrofosmin with a Discovery 570c or Discovery 530c scanner (GE Healthcare, Haifa, Israel). In the external testing populations, patients underwent either a ^{99m}Tc -Sestamibi rest-stress or a ^{99m}Tc -tetrofosmin stress-rest protocol with a Discovery 570c scanner (GE Healthcare, Haifa, Israel). Weight-adjusted (\pm standard deviation [SD]) stress imaging doses of 403 ± 207 MBq (4.8 ± 2.5 MBq/kg, 10.9 ± 5.6 mCi) were used in the training population and 413 ± 157 MBq (5.0 ± 1.9 MBq/kg, 11.2 ± 4.2 mCi) for the external population. Stress images were acquired 15-60 minutes after stress over a total of 4-6 minutes (7). Patients underwent exercise or pharmacologic stress using standard clinical parameters. Details of CT acquisitions and image quality control are available in the supplement.

Model Architecture

The model architecture is outlined in Figure 1. We developed a cGAN which generates simulated AC images (DeepAC). The model was developed using 4886 (train 4398: validation 488) pairs of NC and AC short axis SPECT slices from stress acquisitions from a single site. Our proposed method focuses on CT-free direct estimate of SPECT AC generation and is independent of any imaging information from CT (8). Ground truth short-axis SPECT AC images (reconstructed at 4x4 mm with slice thickness of 4 mm) were used to compare DeepAC. Additional details are available in the Supplement (9-14).

Processing Speed

Batch mode was used for model testing. Using a graphics processing unit (GeForce RTX 2080), the mean time to generate DeepAC images volume from AC volume was 9 milliseconds.

Using a computer similar to a standard reporting workstation (AMD Ryzen 9 5950X 16-Core Processor, 64 Gb RAM), the mean inference time was 66 milliseconds.

Quantitative Image Analysis

All quantitative image comparisons were performed in the external testing population. Stress total perfusion deficit (TPD) was quantified with Quantitative Perfusion SPECT (QPS) software (Cedars-Sinai Medical Center, Los Angeles, CA) (15). Quantification of TPD for DeepAC images was performed using existing sex-specific databases for AC studies. Additionally, we utilized “change” analysis, as implemented in clinical software to perform voxel-by-voxel comparisons between AC, NC, and DeepAC images (16). The “change” analysis allows derivation of positive and negative count change between image pairs (sum of absolute voxel-by-voxel count changes in both directions) without normal databases. Positive change integrates image voxels with an increase in counts on AC images and negative change integrates voxels where AC image has decreased counts compared to NC image. Thus, positive change identifies perfusion defects which are corrected by the reference technique and negative change identifies relative perfusion defects unmasked by the reference technique. Change analysis can be used clinically to detect subtle differences in image sets; for example, when comparing stress and rest images, it could be used to identify areas of ischemia (16). This analysis was also performed on a per-vessel basis.

Diagnostic Accuracy for Obstructive CAD

Diagnostic accuracy was assessed in patients with same-day SPECT and coronary CT angiography (n=280) and low likelihood of coronary disease (LLK) (n=324). Patients from the University of Zurich underwent coronary CT angiography on the same day as SPECT MPI.

Obstructive CAD was defined as any stenosis $\geq 70\%$ or $\geq 50\%$ in the left main coronary artery. To ensure the prevalence of obstructive CAD is similar to that seen in a suspected CAD referral cohort, the population was enriched with a LLK population from the University of Calgary. The LLK population included patients who did not undergo revascularization within 90 days of SPECT MPI and met the following criteria: 1) low-probability of CAD based on the Diamond-Forrester model (17), 2) normal expert visual interpretation of perfusion, 3) coronary artery calcium (CAC) score of 0 and 4) left ventricular ejection fraction $>50\%$. We also evaluated diagnostic accuracy on a per-vessel basis, with left main disease attributed to both the left anterior descending and left circumflex territories.

Statistical Analysis

Standard descriptive statistics were used. Normality for continuous variables was assessed with the Shapiro-Wilks test. Continuous variables were not found to have a normal distribution and difference in median was assessed using the Wilcoxon signed-rank test. The Pitman-Morgan test was used to compare variance between the differences of AC and DeepAC and AC and NC data. Diagnostic accuracy of obstructive CAD was assessed using area under the receiver operating characteristic curve (AUC). DeLong's test was used to evaluate for differences in AUC. Lastly, we evaluated normalcy rates in the LLK population, with abnormal quantitative perfusion defined as stress TPD $> 3\%$ (integer) (4).

All statistical tests were two-sided with $p\text{-value} < 0.05$ considered significant. Statistical analyses were performed using R (version 4.1.2) and Stata/IC version 14.2 (StataCorp, College Station, Texas, USA).

RESULTS

Population Characteristics

Characteristics of the training and external testing populations are shown in Table 1. Patients in the training population were older (median age 64 vs 60 years, $p<0.001$) and more likely to be male (55% vs 48%, $p<0.001$) compared to patients in the testing population.

Diagnostic Accuracy

Obstructive CAD was present in 64/604 (10.6%) patients in the external testing population compared to 10.7% in a large randomized controlled trial (18). Diagnostic accuracy for obstructive CAD is shown in Figure 2. The AUC for DeepAC stress TPD (AUC 0.79, 95% CI 0.62 – 0.85) was higher compared to NC TPD (0.70, 95% CI 0.63– 0.78, $p<0.001$). There was no difference in the AUC of DeepAC TPD compared to AC TPD (AUC 0.81, 95% CI 0.725– 0.87, $p=0.196$). At 80% sensitivity, the specificity of DeepAC TPD was 64% (cut point $\geq 3.3\%$), compared to 65% for AC TPD (cut point $\geq 3.3\%$) and 36% for NC TPD (cut point $\geq 2.0\%$). Using standard previously established threshold of TPD $>3\%$ for abnormal, DeepAC had sensitivity 80% and specificity of 63% compared to sensitivity 78% and specificity 66% for AC TPD and sensitivity 70% and specificity 56% for NC TPD. The normalcy rate at this threshold in the LLK population was higher for DeepAC TPD (70.4%) and AC TPD (75.0%) compared to NC TPD (54.6%, $p<0.001$ for both).

We also assessed diagnostic accuracy for obstructive CAD on a per-vessel level, with results in Supplemental Table 2. The diagnostic accuracy for left anterior descending disease was significantly higher for DeepAC stress TPD (AUC 0.77, 95% CI 0.69-0.86) compared to NC TPD (AUC 0.69, 95% CI 0.59 – 0.79, $p=0.007$). Diagnostic accuracy was also higher for left circumflex

disease for DeepAC stress TPD (AUC 0.74, 95% CI 0.60-0.88) compared to NC TPD (AUC 0.60, 95% CI 0.45 – 0.76, $p=0.024$).

Comparison of AC, NC, and DeepAC SPECT Images

Results of the change analysis is shown in Figure 3. Positive change was significantly lower, representing closer agreement, for AC vs DeepAC (median 2.4, IQR 1.3 – 4.2) compared to AC vs NC (median 9.4, IQR 6.0 – 14.2, $p<0.001$). However, negative change was similar for AC vs DeepAC (median 2.0, IQR 0.9 – 3.5) compared to AC vs NC (median 2.0, IQR 1.2 – 3.6, $p=0.935$). Similar findings were seen in the subset of patients undergoing stress-first imaging for positive change (AC vs DeepAC median 2.6, IQR 1.6 – 4.9; AC vs NC median 12.9, IQR 8.5 – 17.8, $p<0.001$) and negative change (AC vs DeepAC median 2.7, IQR 1.5 – 5.1; AC vs NC median 2.5, IQR 1.5 – 4.2, $p<0.001$). Results of the per-vessel change analysis are shown in Supplemental Figure 1. Median positive change was significantly higher with AC vs NC compared to AC vs DeepAC in the left anterior descending (2.61 vs 2.02), left circumflex (4.22 vs 0.32) and right coronary artery territories (18.96 vs 1.18, $p<0.001$ for all).

Absolute differences between AC TPD vs DeepAC TPD were lower compared to the absolute differences between AC TPD and NC TPD (median 1.2 vs 2.3, $p<0.001$) (Figure 4). The Bland-Altman analysis for TPD is outlined in Supplemental Figure 2. Limits of agreement for AC TPD vs DeepAC TPD (bias -0.2, 95% limits of agreement -6.5 to 6.1; Spearman's Rho 0.78) were closer compared AC TPD vs NC TPD (bias -1.0, 95% limits of agreement -8.7 to 6.7; Spearman's Rho 0.55; $p<0.001$).

Case Examples

Cases illustrating AC, DeepAC, and NC images as well as the concept of positive change analysis are shown in Figures 5-7.

DISCUSSION

We developed a cGAN deep learning model, which directly generates DeepAC images, without CT, from NC images. It eliminates the possibility of CT misregistration, leverages optimized vendor-specific reconstruction algorithms for dedicated collimators and solid-state scanners, and allows physicians to evaluate full image sets for potential artifacts using the same approaches they would for any other clinical study. The model generates DeepAC images in a fraction of a second on standard computer hardware and could readily be implemented in clinical workflows as an automatic pre-processing step.

Critically, we demonstrate that the diagnostic accuracy of DeepAC was higher compared to NC using a large, external testing population. Additionally, using clinical quantitative analysis, we conclusively demonstrate that DeepAC images are more similar to AC images compared to NC images. The significant improvement in positive change suggests that DeepAC corrects attenuation artifacts relative to NC images. Importantly, similar findings were seen in the subset of patients undergoing stress-first imaging, which typically are noisier images. While the absence of difference in negative change suggests that it is not inducing (or uncovering) defects in a manner that would not be expected with actual AC. DeepAC could be applied clinically in laboratories without dedicated SPECT/CT hardware (majority of SPECT MPI laboratories) to increase normalcy rates and diagnostic accuracy, without affecting existing imaging protocols.

Several AI approaches have been proposed recently to generate simulated AC SPECT MPI (9,19-21). Nguyen et al. developed a generative adversarial network (GAN) to simulate AC images from non-AC data with data from 491 patients for training and 112 for testing, demonstrating higher structural similarity index compared to 3D UNet (19). Chen et al. proposed a dual squeeze and excitation residual dense network, trained and tested with 172 studies, using images from 3 scatter windows together with NC images to predict AC images (9). Yang et al. developed a convolutional network to generate simulated AC images directly from NC images using 100 paired datasets for training and testing and 10-fold cross-validation (20). In the only other study, which evaluated the clinical impact of the deep learning AC, Hagio et al. developed a convolutional network which generates simulated AC polar maps from NC maps (rather than images) (21). The authors trained and trained and tested the model in a population from a single center, demonstrating improvement in diagnostic accuracy for CAD in patients with either correlating angiography (n=351) or LLK cases (n=327). Improvement in specificity was 26% (higher quality studies) and 8% (lower quality studies) in internal testing. However, none of these studies included external testing populations. In the present work, we show higher diagnostic accuracy with DeepAC compared to NC images and up to 28% higher specificity, in a large external testing population from two different sites using standard clinical quantification of SPECT MPI. We also show improved similarity between AC and DeepAC SPECT images as compared to NC images.

There are several aspects of our work which are particularly relevant to the future clinical application of the DeepAC model. Our model generates simulated SPECT short-axis images, rather than corrected polar maps. This allows physicians to identify potential sources of artifact such as excessive gut activity and potential errors in myocardial contours. We did not need to exclude cases with surface mismatch or segmentation errors as was needed in previous polar map-

based approaches (21). Our approach leverages existing vendor-specific reconstruction algorithms and could be implemented as a pre-processing step prior to interpretation with any SPECT MPI interpretation software (22). Importantly, in an independent population, we demonstrated that DeepAC improved diagnostic accuracy for obstructive CAD and normalcy rates, compared to NC SPECT. We used a very conservative definition of low-likelihood, including CAC score of 0 (23), to minimize any chance of misclassifying presence of obstructive CAD in the absence of defined coronary anatomy. We believe this is the first time the utility of simulated AC was demonstrated conclusively with independent, external testing—a critical step towards demonstrating the generalizability of the technique.

DeepAC could be applied clinically to correct for photon attenuation without the additional radiation exposure, cost, and space required for hybrid SPECT/CT. The algorithm could be applied to correct NC SPECT MPI in sub-second times, avoiding potential issues with image mis-registration. Importantly, it could be combined with stress-first imaging. We have previously demonstrated that AI can identify low-risk patients for rest scan cancellation (24). DeepAC imaging could be used to further improve the accuracy of these algorithms.

Our study has a few important limitations. Validation of DeepAC on other SPECT camera systems is needed. Further improvements in diagnostic accuracy may be possible by applying dedicated DeepAC databases. Additionally, we did not assess the performance of the DeepAC model on rest images. While DeepAC allows for soft-tissue AC, it does not provide the additional anatomic information available from CTAC, such as calcium. Therefore, the benefits of implementing this technique to reduce radiation exposure against the added clinical information available from continuing with CTAC imaging need to be carefully weighted (25). Lastly, while

the population level results show improved diagnostic accuracy, physicians will still need to review all available data to ensure that the DeepAC results make sense clinically.

CONCLUSIONS

We developed a deep learning model which generates DeepAC images from NC reconstructed short-axis slices. DeepAC images provide more similar quantitative assessment of perfusion to actual AC images compared to NC images. This translates into improved diagnostic accuracy for obstructive CAD in external testing. DeepAC may simplify the task of artifact identification for physicians compared to NC images alone and can be performed without the need for CTAC hardware.

SOURCE OF FUNDING

This research was supported in part by grant R01HL089765 and R35HL161195 from the National Heart, Lung, and Blood Institute/ National Institutes of Health (NHLBI/NIH) (PI: Piotr Slomka). The content is solely the responsibility of the authors and does not necessarily represent the official views of the National Institutes of Health.

DISCLOSURES

Dr. Robert Miller has received consulting fees and research support from Pfizer. Drs. Berman and Slomka and Mr. Kavanagh participate in software royalties for QPS software at Cedars-Sinai Medical Center. Dr. Berman is a consultant for GE Healthcare and Dr. Edward Miller has served as GE Healthcare consultant. Dr. Slomka has received research grant support from Siemens Medical Systems. The remaining authors have no relevant disclosures.

KEY POINTS

QUESTION:

Can deep-learning be used to generate AC SPECT images directly from non-AC images?

PERTINENT FINDINGS:

We developed a method to generate simulated AC images (DeepAC) and compared them to actual AC and non-AC images using a large external testing population. DeepAC images were more similar to actual AC images compared to non-AC images and had similarly high diagnostic accuracy as actual AC images.

IMPLICATIONS FOR PATIENT CARE:

The DeepAC model could be applied clinically to generate AC image sets, on SPECT systems without CT capability for improved diagnostic accuracy or to help identify patients for rest-scan cancellation.

REFERENCES

1. Berman DS, Hachamovitch R, Kiat H, et al. Incremental value of prognostic testing in patients with known or suspected ischemic heart disease. *J Am Coll Cardiol.* 1995;26:639-647.
2. Otaki Y, Betancur J, Sharir T, et al. 5-year prognostic value of quantitative versus visual MPI in subtle perfusion defects. *JACC Cardiovasc Imaging.* 2020;13:774-785.
3. Huang JY, Huang CK, Yen RF, et al. Diagnostic performance of attenuation-corrected myocardial perfusion imaging for coronary artery disease. *J Nucl Med.* 2016;57:1893-1898.
4. Arsanjani R, Xu Y, Hayes SW, et al. Comparison of fully automated computer analysis and visual scoring for detection of coronary artery disease from myocardial perfusion spect in a large population. *J Nucl Med.* 2013;54:221-228.
5. van Dijk JD, Mouden M, Ottervanger JP, et al. Value of attenuation correction in stress-only myocardial perfusion imaging using CZT-SPECT. *J Nucl Cardiol.* 2017;24:395-401.
6. Kennedy JA, Israel O, Frenkel A. Directions and magnitudes of misregistration of CT attenuation-corrected myocardial perfusion studies: incidence, impact on image quality, and guidance for reregistration. *J Nucl Med.* 2009;50:1471-1478.
7. Dorbala S, Di Carli MF, Delbeke D, et al. SNMMI/ASNC/SCCT guideline for cardiac SPECT/CT and PET/CT 1.0. *J Nucl Med.* 2013;54:1485-1507.
8. Torkaman M, Yang J, Shi L, et al. Direct image-based attenuation correction using conditional generative adversarial network for SPECT myocardial perfusion imaging. *Proc SPIE Int Soc Opt Eng.* 2021;11600:116000U.
9. Chen XC, Zhou B, Shi LY, et al. CT-free attenuation correction for dedicated cardiac SPECT using a 3D dual squeeze-and-excitation residual dense network. *J Nucl Cardiol.* 2021;Epub ahead of print.
10. Jin Q, Meng Z, Sun C, Cui H, Su R. RA-UNet: a hybrid deep attention-aware network to extract liver and tumor in CT scans. *Front Bioeng Biotechnol.* 2020;8:605132.
11. Isola P, Zhu J, Zhou T, Efros AA. Image-to-image translation with conditional adversarial networks. *IEEE Conf Comput Vis Pattern Recog.* 2017;1:21-27.
12. Johnson J, Alahi A, Fei-Fei L. Perceptual losses for real-time style transfer and super-resolution. *ECCV Conf Comput Vis.* 2016;1:1-10.
13. Kumar SK. On weight initialization in deep neural networks. *arXiv.* 2017.
14. Kingma DP, Adam BJ. A method for stochastic optimization. *arXiv.* 2014

15. Slomka PJ, Nishina H, Berman DS, et al. Automated quantification of myocardial perfusion SPECT using simplified normal limits. *J Nucl Cardiol*. 2005;12:66-77.
16. Slomka PJ, Nishina H, Berman DS, et al. Automatic quantification of myocardial perfusion stress–rest change: a new measure of ischemia. *J Nucl Med*. 2004;45:183-191.
17. Diamond GA, Forrester JS. Analysis of probability as an aid in the clinical diagnosis of coronary-artery disease. *N Engl J Med*. 1979;300:1350-1358.
18. Douglas PS, Hoffmann U, Patel MR, et al. Outcomes of anatomical versus functional testing for coronary artery disease. *N Engl J Med*. 2015;372:1291-1300.
19. Nguyen TT, Chi TN, Hoang MD, Thai HN, Duc TN. 3D Unet generative adversarial network for attenuation correction of SPECT images. *Sig Proc Telecomm*. 2020;8-19.
20. Yang J, Shi L, Wang R, et al. Direct attenuation correction using deep learning for cardiac SPECT: a feasibility study. *J Nucl Med*. 2021;62:1645-1652.
21. Hagio T, Poitrasson-Rivière A, Moody JB, et al. “Virtual” attenuation correction: improving stress myocardial perfusion SPECT imaging using deep learning. *Eur J Med Mol Imaging*. 2022;Epub ahead of print.
22. Slomka P, Miller RJ, Hu L-H, Germano G, Berman D. Solid-state detector SPECT myocardial perfusion imaging. *J Nucl Med*. 2019;60:1194-1204.
23. Budoff MJ, Blankstein R, Nasir K, Blaha MJ. Power of zero stronger than soft plaque. *J Cardiovasc Comput Tomogr*. 2020;14:279.
24. Hu LH, Miller RJH, Sharir T, et al. Prognostically safe stress-only single-photon emission computed tomography myocardial perfusion imaging guided by machine learning: report from REFINE SPECT. *Eur Heart J Cardiovasc Imaging*. 2021;22:705-714.
25. Trpkov C, Savtchenko A, Liang Z, et al. Visually estimated coronary artery calcium score improves SPECT-MPI risk stratification. *Int J Cardiol Heart Vasc*. 2021;35:100827.

FIGURES

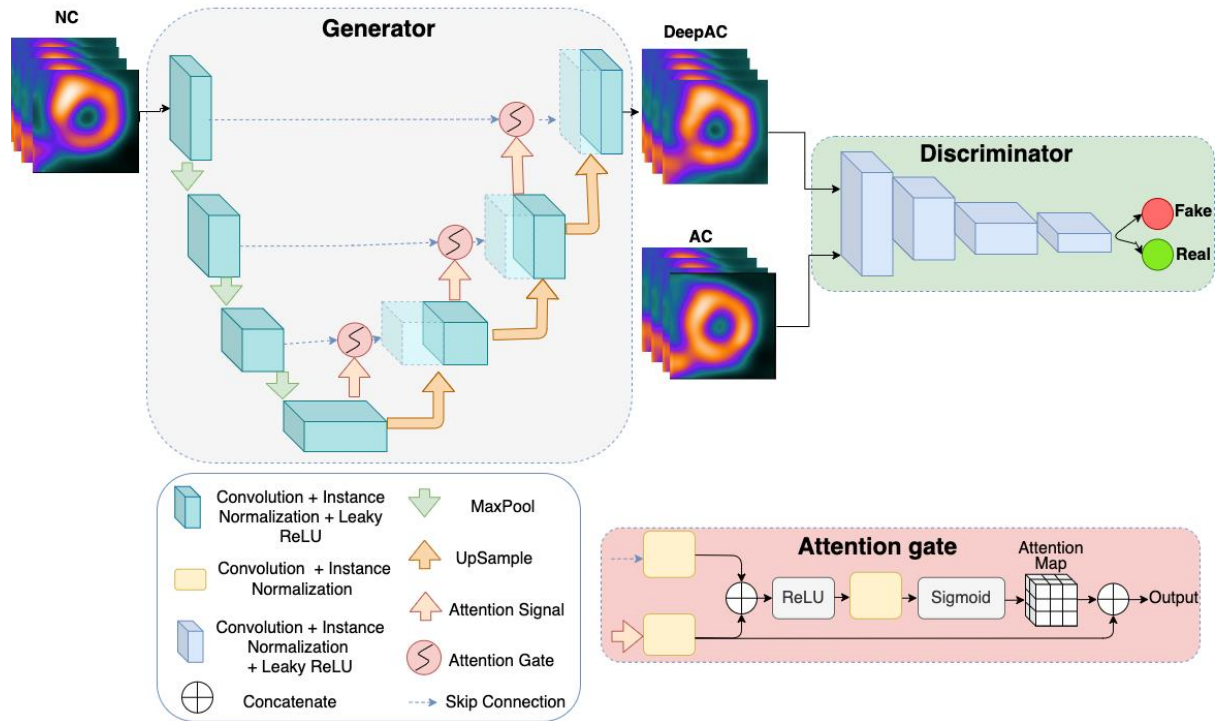


FIGURE 1: Model Architecture. The model is a conditional generator adversarial network. First the generator network creates simulated attention corrected (AC) images from non-corrected (NC) images. The discriminator (green box) is tasked with differentiating actual AC images (real) from DeepAC images (fake). The generator (grey box) is an attention-gated 3D UNet where maximum pooling (MaxPool) downsamples the features. The attention gate (red box) takes input from the lower level (attention signal) with the skipped connection; it includes a rectified linear unit (ReLU) as a non-linear activation and generates an attention map which is concatenated to the upsampled level. This helps the generator network focus on essential image structures.

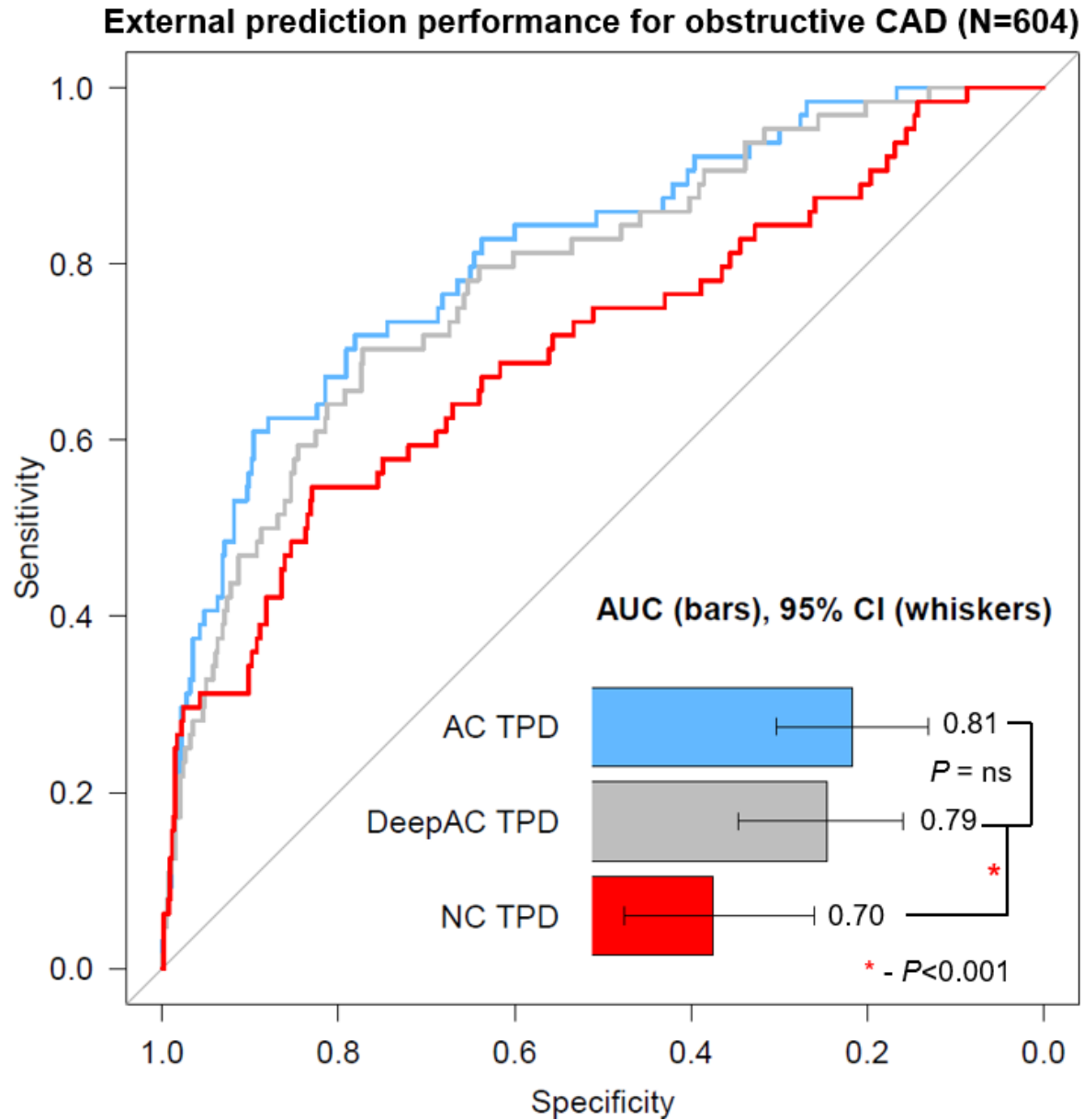


FIGURE 2: Diagnostic accuracy for obstructive coronary artery disease (CAD). The area under the receiver operating characteristic curve (AUC) for AC (blue) and DeepAC (grey) stress total perfusion deficit (TPD) was higher compared to non-attenuation corrected (NC) stress TPD (red). There was no significant (ns) difference between DeepAC stress TPD and AC stress TPD (blue).

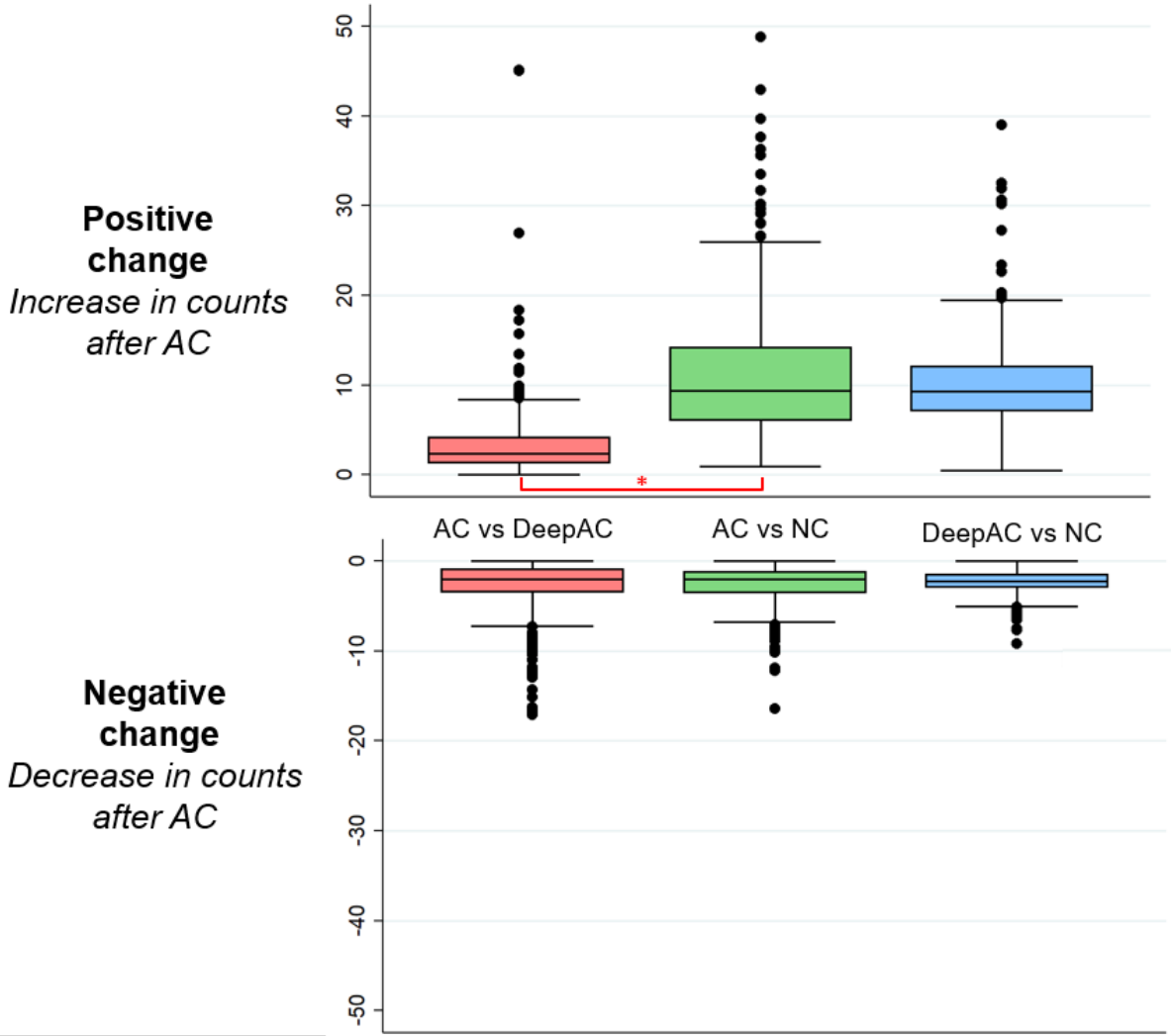


FIGURE 3: Change analysis (voxel-by-voxel analysis after subtraction of co-registered images). Actual attenuation corrected (AC) images were the reference image for comparisons of AC vs DeepAC (red) and AC vs non-attenuation corrected (NC) images (green). DeepAC was used as the reference for DeepAC vs NC (blue). Negative change was not significantly different across all comparisons. However, positive change was significantly lower for AC vs DeepAC compared to AC vs non-attenuation corrected images (* $p < 0.001$).

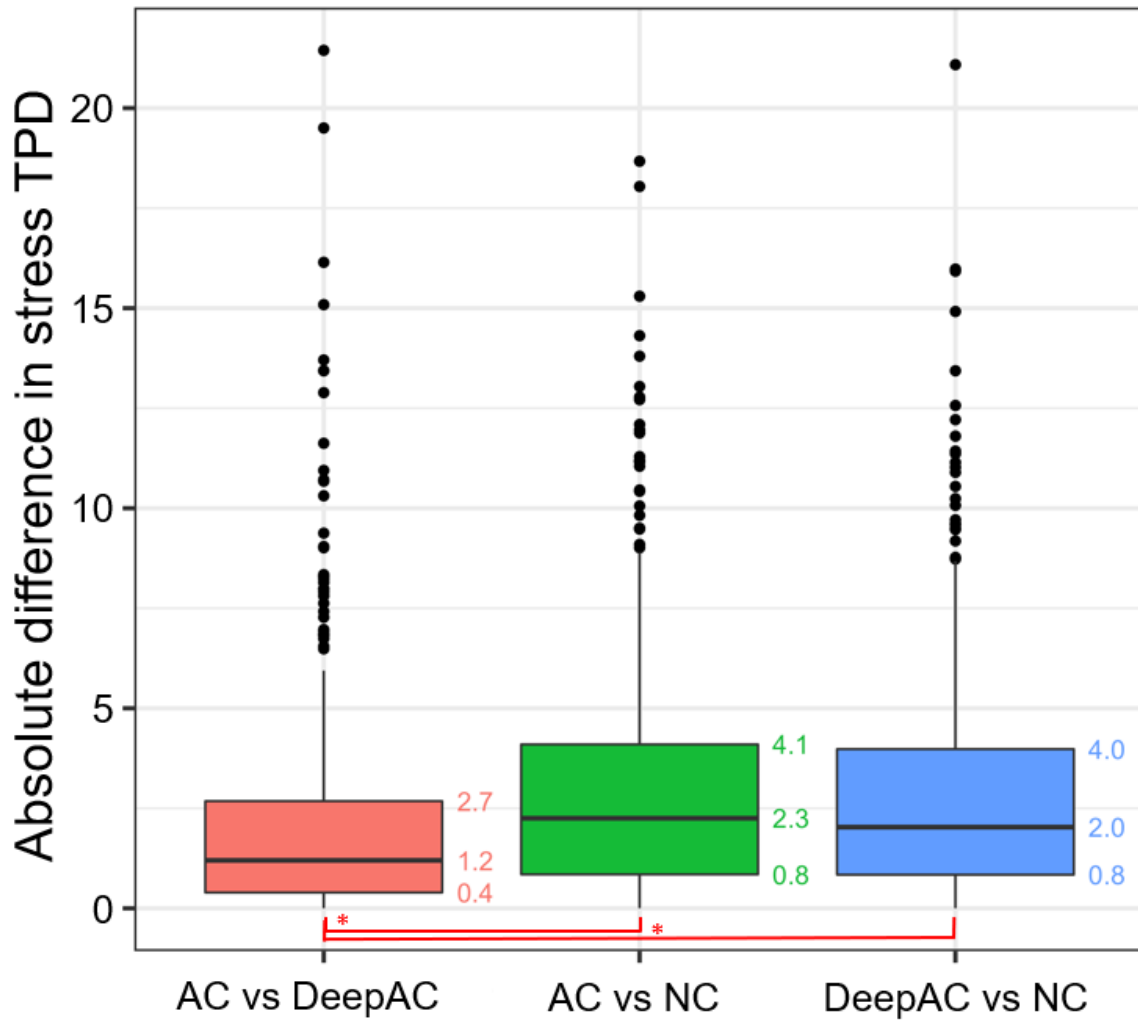


FIGURE 4: Absolute differences in stress total perfusion deficit (TPD) between attenuation corrected (AC), DeepAC, and non-attenuation corrected (NC) values. Median absolute difference was lower for AC vs DeepAC (red), compared to AC vs NC (green) or DeepAC vs NC (blue) (both * $p < 0.001$).

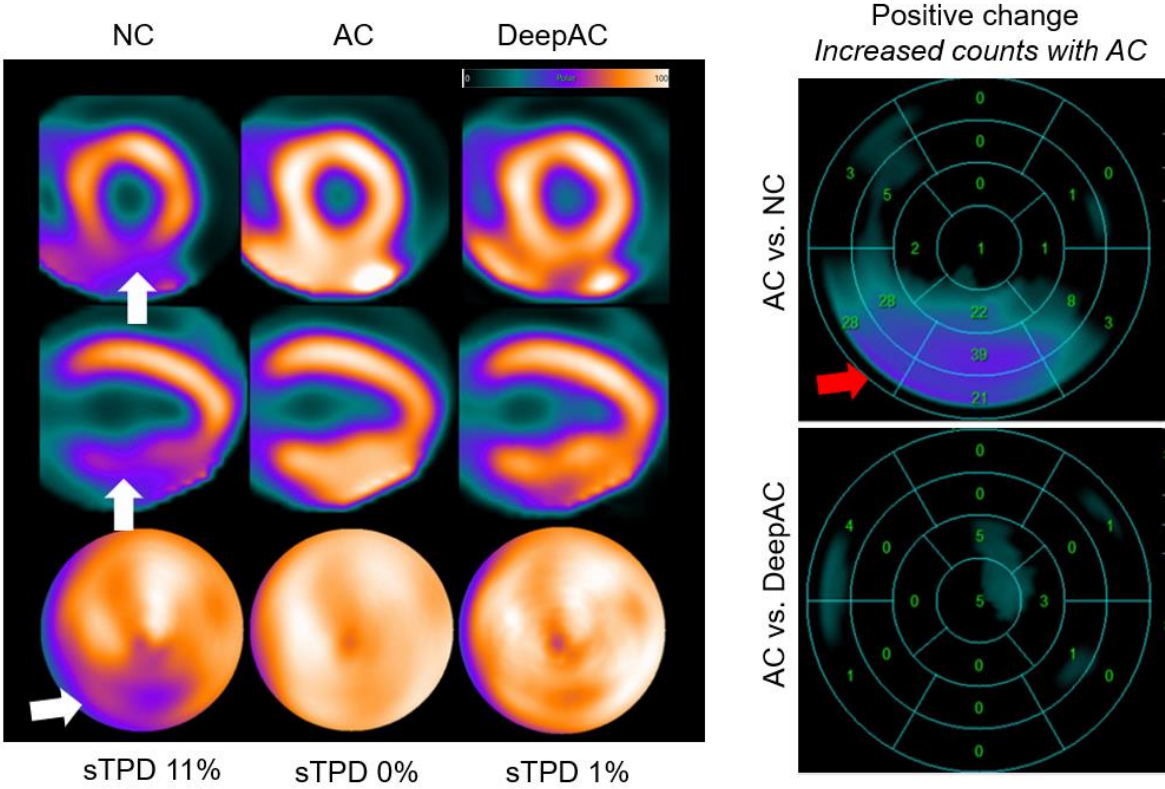


FIGURE 5: Non-attenuation corrected (NC), attenuation corrected (AC) and DeepAC images from a 53-year-old man with body mass index of 36. On short-axis images (top), vertical long axis (middle), and polar maps (bottom) there was a defect in the inferior wall on NC images only (white arrows), with evidence of adjacent radiotracer activity in the abdomen. Standard quantification by stress total perfusion deficit (sTPD) was 11% (abnormal). After AC correction, the sTPD was 0%, DeepAC correction resulted in sTPD 1% (both normal). There was a positive change of inferior wall counts for AC vs NC (red arrow). There was no change seen between AC vs DeepAC images. The patient had no coronary artery disease on coronary computed tomography angiography and the defect most likely represents diaphragmatic attenuation.

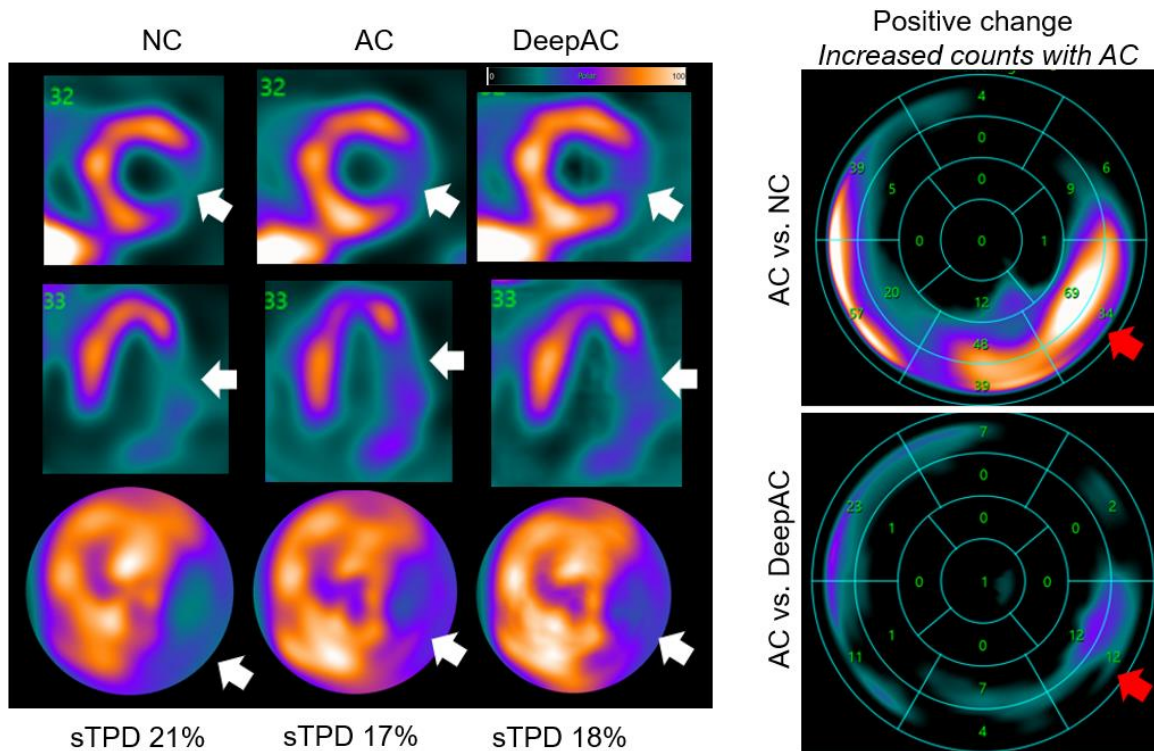


FIGURE 6: Non-attenuation corrected (NC), attenuation corrected (AC) and DeepAC images from a 63-year-old woman with body mass index of 32. On short-axis images (top), vertical long axis (middle) and polar maps (bottom) there was a defect in the anterolateral, inferolateral, and inferior walls on NC images (white arrows). Standard quantification by stress total perfusion deficit (sTPD) was 21% (abnormal). After AC correction, the sTPD was 17%, DeepAC correction resulted in sTPD 18% (both abnormal). There was positive change in the inferior and inferoseptal walls for AC vs NC (red arrows). There was a only a small area of positive change in the inferolateral wall for AC vs DeepAC. The patient had an 80% stenosis of the proximal left circumflex.

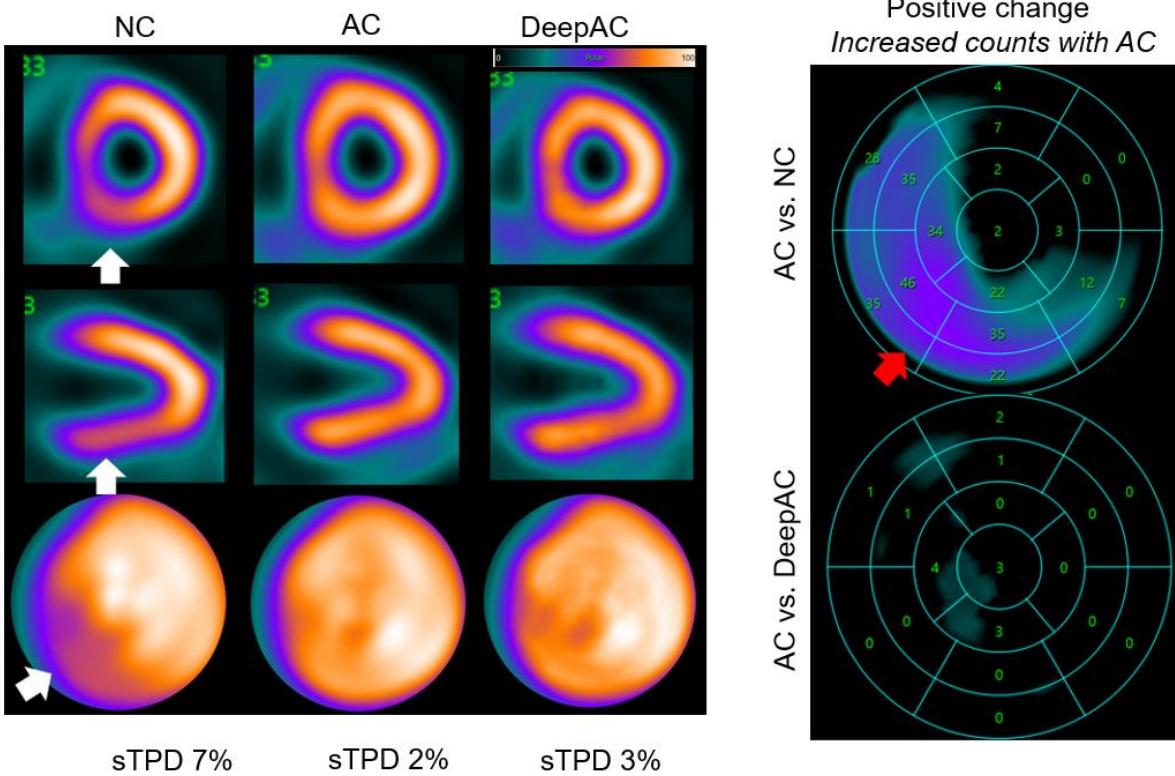


FIGURE 7: Non-attenuation corrected (NC), attenuation corrected (AC) and DeepAC images from a 62-year-old woman with body mass index of 29. On short-axis images (top), vertical long axis (middle) and polar maps (bottom) there was a defect in the inferior and inferoseptal walls on NC images only (white arrows). Standard quantification by stress total perfusion deficit (sTPD) was 7% (abnormal). After AC correction, the sTPD was 2%, DeepAC correction resulted in sTPD 3% (both normal). There was a positive change of inferior and inferoseptal wall counts for AC vs NC (red arrow). There was no change seen between AC vs DeepAC images. The patient had no coronary artery disease on coronary computed tomography angiography.

TABLES

Table 1:

Characteristic	Training Population (N = 4,886)	External Testing N=604	p-value
Age, median (IQR)	64(56, 73)	60(53, 68)	<0.001
Male, n(%)	2,705(55)	341(48)	<0.001
BMI, median (IQR)	29(26, 34)	28(25, 32)	<0.001
Past Medical History, n(%)			
Hypertension	3,204(67)	255(36)	<0.001
Diabetes Mellitus	1,292(27)	71(10)	<0.001
Dyslipidemia	2,649(55)	195(28)	<0.001
History of CAD	873(18)	67(9)	<0.001
Stress test type, n(%)			
Exercise	1,775(36)	393(56)	<0.001
Pharmacologic	3,106(64)	313(44)	<0.001

TABLE 1: Population characteristics of the training and external testing populations. BMI -body mass index, CAD – coronary artery disease, CCTA- coronary computed tomography angiography, IQR – interquartile range.